

Chapter 6

Ambient seismic noise tomography at Ekofisk

In Chapter 2 to 5 I presented an extensive characterization of noise and noise correlations for ambient seismic recordings made at Valhall. Here I study an almost 40-hour recording from the Life of Field Seismic (LoFS) array installed over Ekofisk field, to assess whether passive seismic interferometry leads to success at other OBC arrays. The noise recorded by the pressure-sensors between 0.4 and 1.2 Hz consists mostly of Scholte-wave microseism energy. The noise incidence directions have an almost uniform distribution over azimuth, enabling the synthesis of symmetric Estimated Green's Functions (EGFs). These results are significant because they show that recordings made at the Ocean-Bottom Cable (OBC) array at Ekofisk field in the absence of seismic shooting can be used to image the near surface. A dispersion analysis shows that the Scholte-wave virtual seismic source exhibits a peak sensitivity between 160 and 730 m below the sea floor. Straight-ray group-velocity tomography locates a high-velocity anomaly in the center of Ekofisk's production-induced subsidence bowl, surrounded by a lower-velocity region.

INTRODUCTION

Since 2010, Ekofisk field has had a Life of Field Seismic (LoFS) four-component optical sensor array installed over the North Sea field (Eriksrud, 2010). The main objective is to record during active seismic surveying for production-related time-lapse surveying (Folstad et al., 2010).

A preliminary study of an ocean-bottom-node (OBN) recording over the Astero field yielded images of group velocities between 0.18 Hz and 0.4 Hz, with correlation to known structures (Bussat and Kugler, 2011). Ocean-bottom-cable (OBC) ambient noise recordings made by a LoFS installation over Valhall field have yielded images of the near surface using Scholte-wave group and phase velocities between 0.5 and 1.75 Hz (de Ridder and Dellinger, 2011). Both studies utilize energy from the double-frequency microseism band excited by swell noise (Longuet-Higgins, 1950). In marine environments this energy is dominated by Scholte waves (Olofsson, 2010). Over land this energy peak is composed of surface and body waves incident from coasts and shallow seas (Ruigrok et al., 2011).

Here, I present a study of almost 40 hours of data recorded by the pressure sensors of the LoFS at Ekofisk field and investigate whether Scholte-wave group-velocity ambient noise tomography can be successfully applied at Ekofisk. I find that the microseism energy recorded between 0.4 Hz and 1.2 Hz contains sufficient Scholte-wave energy to yield Scholte-wave virtual seismic sources obtained from crosscorrelation. Scholte-wave group-velocity maps for five central frequency ranges, from 0.4 – 0.6 Hz to 1.2 – 1.4 Hz, are inverted by straight-ray tomography.

AMBIENT SEISMIC FIELD RECORDED BY LOFS AT EKOFISK FIELD

In this section I analyse the characteristics of the microseism noise recorded by the pressure sensors of Ekofisk’s LoFS array. Figure 6.1 contains a map with the LoFS station locations in (a) and the bathymetry of the sea floor in (b). Rapid pressure

depletion in the early phase of production and weakening due to subsequent water injection caused over 9 meters of sea-floor subsidence over the Ekofisk field (Hermansen et al., 1997; Lyngnes et al., 2013). The in-line and cross-line station spacings are approximately 50 m and 300 m, respectively. The array comprises approximately 3950 stations. For this study, I received a dataset spanning 41 hours, 28 minutes and 40 seconds, starting on October 24, 2011, at UTC 00:17:00. There is a gap in the recording lasting about 1 hour and 24 minutes before noon on October 24.

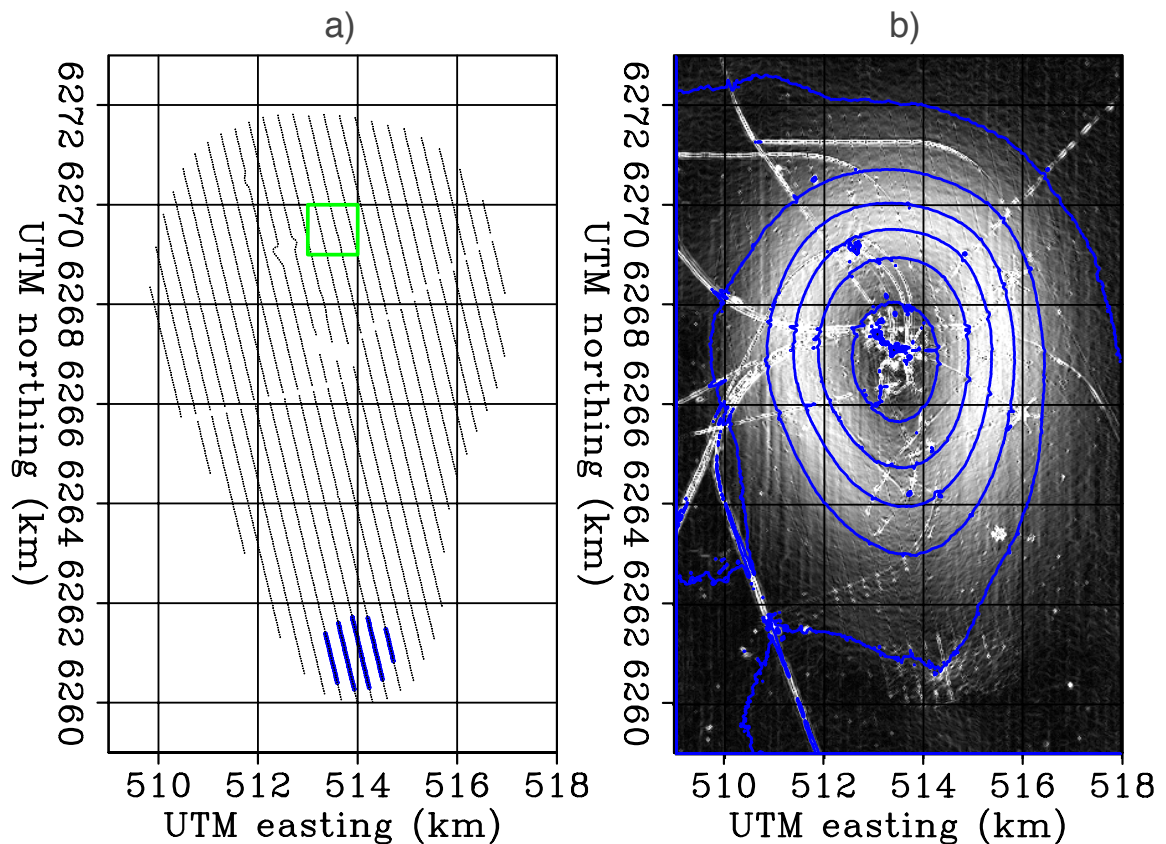


Figure 6.1: a) Map of station locations in Ekofisk's LoFS array (coordinates in ED50 / UTM Zone 31N). Each black dot denotes a station. The stations used to create the spectrogram in Figure 6.2 and for the beam steering results in Figure 6.3 are shown in blue. The common midpoints for the dispersion analysis in Figure 6.5 are denoted by the green square. b) Bathymetry map of the sea floor at Ekofisk field, 2 m contour levels. The gray-scale shading indicates the magnitude of the bathymetry gradient.

[ER] ekofisk-array

The transient nature of the ambient seismic field is observed in the spectrogram shown in Figure 6.2. This spectrogram is computed by Fourier transformation of 2.5-minute recording windows with 50% overlap. The spectrogram was averaged over a subset of 119 stations located in a radius of 750 m of UTM (514 km east, 6261 km north), depicted as blue stations in Figure 6.1a.

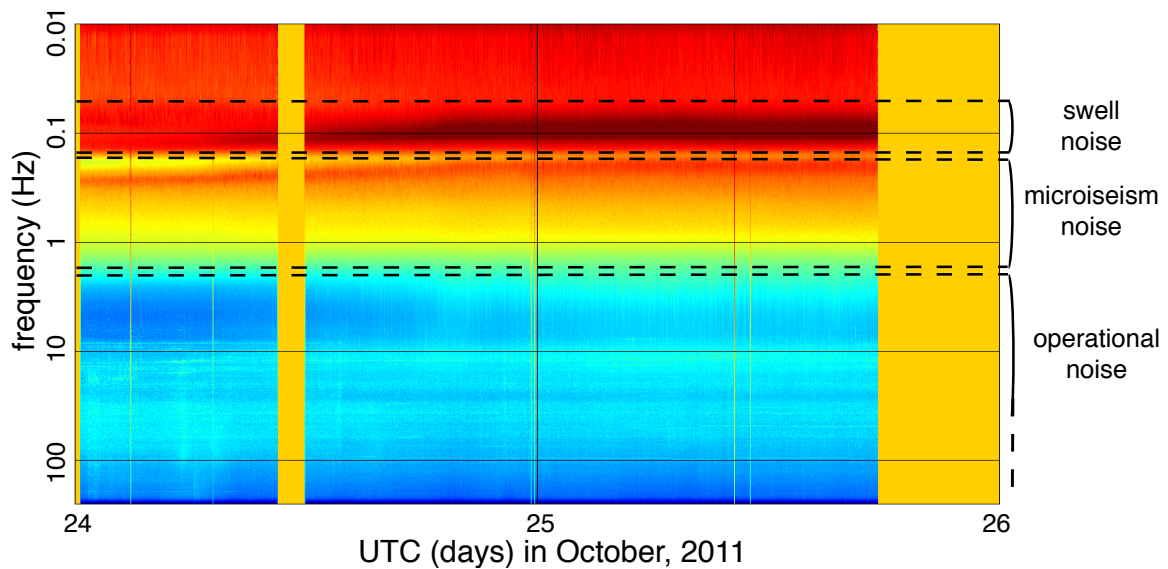


Figure 6.2: Spectrogram showing spectral amplitudes versus time for the duration of the entire recording used in this study. Dashed lines indicate the frequency regimes where swell-noise, microseism-noise and operational noise dominate. Notice that both the microseism energy and swell-noise energy grow stronger during October 24th and remain strong during October 25th. [CR] spectrogram

Analysis of Figure 6.2 identifies three frequency regimes. Below 0.15 Hz the recordings are dominated by ocean swells. These are wind-generated gravity waves in the sea (Munk, 1950). Between 0.35 – 1.35 Hz microseism energy dominates the recordings. Microseism noise is caused by constructively interfering ocean swells that give rise to pressure variations on the sea floor. These pressure variations excite interface waves traveling along the sea floor at approximately twice the frequency of the swell noise (Longuet-Higgins, 1950). Notice that the microseism noise increases when the ocean-swells grow stronger. Above 1.5 Hz, a variety of predominantly field-operational noise sources dominate the recordings. This study focuses on the microseism noise because

Scholte waves travel along the sea floor and provide subsurface sensitivity to the top few hundred meters immediately below the sea floor.

Beam steering is one technique to reveal the azimuth and apparent slowness of energy incident on an array. Beam steering is carried out using the same 119 stations used for the spectrogram (the blue stations in Figure 6.1). The recordings are first filtered for the microseism energy between 0.55 – 0.65 Hz using a Hann taper in the frequency domain. A narrow-frequency band was needed because velocity dispersion causes blurring in the beam steering results. The data are then transformed to the $\tau - p$ domain by slant stack. I take the absolute value and smooth by a triangle over 10 minutes, forming a smooth movie of amplitudes over p_x and p_y as a function of τ . Figure 6.3 contains 13 frames of the movie formed by averaging 2.5 minutes at three-hour intervals. High amplitudes (red) indicate the slowness and azimuth of incoming energy while low amplitudes (blue) indicate the absence of energy. I observe a circle at absolute slowness $|\mathbf{s}| \approx 1.9$ ms/m, corresponding to a velocity of $|\mathbf{s}|^{-1} \approx 525$ m/s. These are the Scholte waves, which travel in many directions and compose the microseism noise of the ambient seismic field. Notice that the noise is remarkably omnidirectional.

PASSIVE SEISMIC INTERFEROMETRY

Ekofisk’s LoFS array has approximately 3950 stations that record particle velocity and pressure two meters below the sea floor. Here, crosscorrelations between the pressure sensor recordings made at all stations were computed. The derivation for the seismic interferometry result of crosscorrelating recordings of particle velocities is included in Appendix A. Let $G^{\bar{p},\bar{q}}(\mathbf{x}_A, \mathbf{x}_B, \omega)$ denote the frequency-domain elastodynamic Green’s function of a composite-receiver recording pressure, \bar{p} , at \mathbf{x}_A due to a composite-source representing a volume injection rate, \bar{q} , at \mathbf{x}_B . An estimate of the Green’s function $G^{\bar{p},\bar{q}}(\mathbf{x}_A, \mathbf{x}_B, \omega)$ and its reciprocal $G^{\bar{p},\bar{q}*}(\mathbf{x}_B, \mathbf{x}_A, \omega)$ can be retrieved as follows:

$$\left\langle \bar{p}(\mathbf{x}_A, \omega) \bar{p}^*(\mathbf{x}_B, \omega) \right\rangle \propto \{G^{\bar{p},\bar{q}}(\mathbf{x}_A, \mathbf{x}_B, \omega) + G^{\bar{p},\bar{q}*}(\mathbf{x}_B, \mathbf{x}_A, \omega)\} S(\omega), \quad (6.1)$$

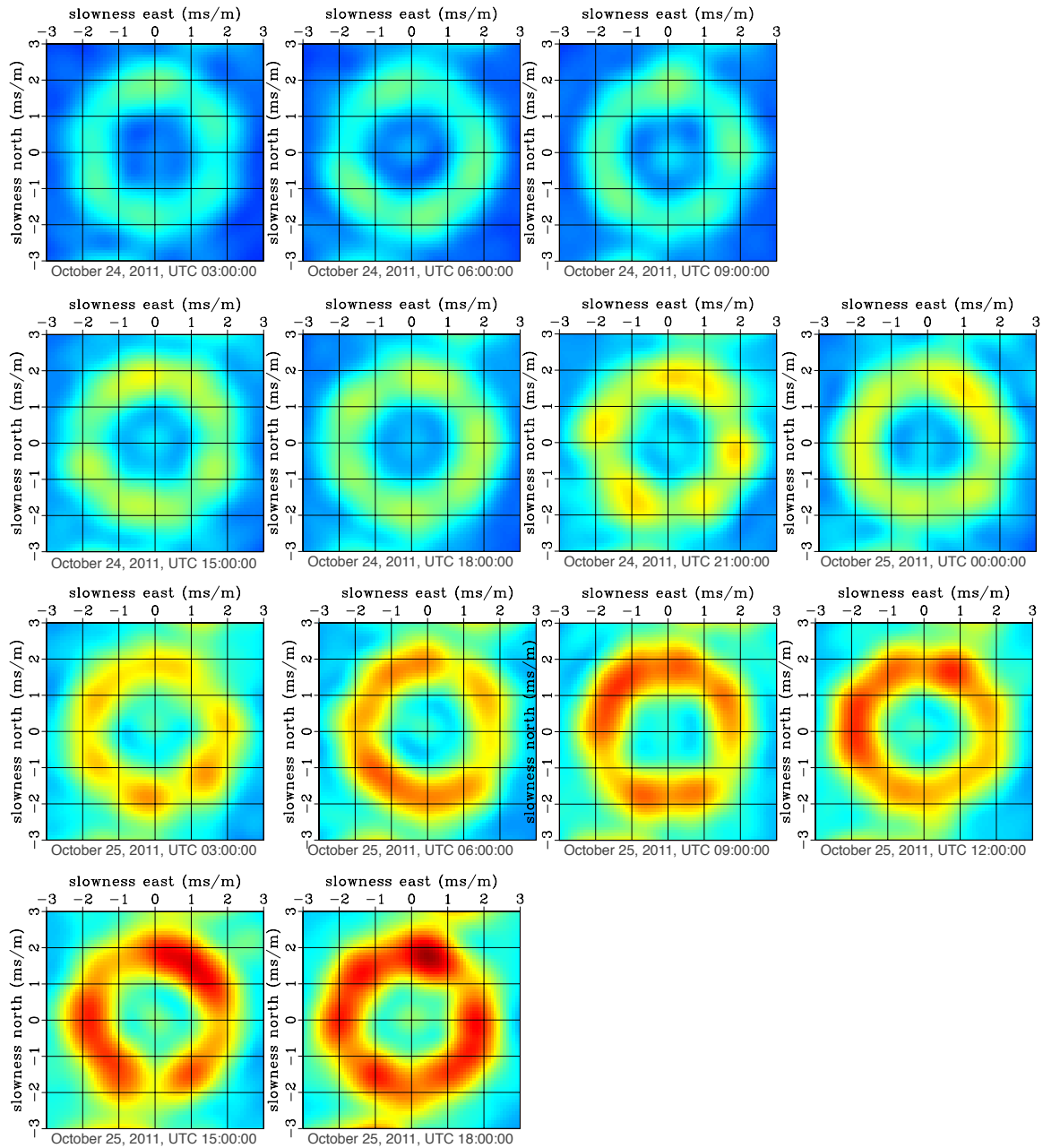


Figure 6.3: Results from beam steering of data filtered between 0.55 – 0.65 Hz, selecting microseism noise. Each image contains a beam steering result from data 3 hours apart and indicate the slowness and azimuth of incoming Scholte-wave energy averaged over 10 minutes. The empty upper-right corner corresponds to missing data on October 24th. [CR] ekofisk-beams

where the crosscorrelated signals $\bar{p}(\mathbf{x}_A, \omega)$ and $\bar{p}(\mathbf{x}_B, \omega)$ denote the pressure recordings made at \mathbf{x}_A and \mathbf{x}_B (the master station), respectively. Complex conjugation is denoted by $*$, and $\langle \rangle$ denotes a spatial ensemble average. The power spectrum of the noise source signals is denoted by $S(\omega)$. The crosscorrelation signal approaches an equivalence of the superposition of the causal Green's function and its anti-causal reciprocal counterpart, forming a purely symmetric signal. Thus, the crosscorrelation signal is referred to as an estimated Green's function (EGF). An estimate for the phase of the Green's function can be found by applying the Heaviside step function to the crosscorrelation signal either before or after symmetrizing. Repeating this procedure for each component at each station in the array with each component at a master station yields an estimated Green's matrix (EGM) for each station pair, collectively called a virtual seismic survey.

VIRTUAL SOURCES FROM EKOFISK'S LOFS ARRAY

To extract the microseism noise and compress the data volume, the recorded pressure data was first filtered using a frequency-domain taper with a flat response for 0.4-1.3 Hz, and a Hann-taper extending from 0.35 Hz to 1.35 Hz. Filtering was done in segments of 3 minutes, plus 20 seconds of overlap, and the data were restitched after filtering and down-sampling. Segments containing noise bursts and spikes were discarded. All available data were then crosscorrelated in 10 blocks of 4 hours. See Appendix B for how to compute cross spectra and their appropriate unit. For each station pair, the crosscorrelations were stacked to form a virtual seismic survey with virtual sources at all stations in Ekofisk's LoFS array. Figure 6.4 shows an example of a virtual seismic source. Figures 6.4a to 6.4e contain the symmetric part of the crosscorrelation signal, while Figures 6.4f to 6.4j contain the antisymmetric part. There is very little coherent energy in the antisymmetric part, and the background correlation fluctuations in the antisymmetric part are on the order of the background correlation fluctuations in the symmetric part. The beam steering results indicate that the noise incidence-directions, especially when averaged over a long time, have uniform distribution over azimuth. But the lack of (almost) any antisymmetric part in the

Frequency (Hz)	0.4	0.5	0.6	0.7	0.8	0.9	1.0	1.1	1.2
Phase velocity (m/s)	584.1	565.6	525.2	490.2	466.4	448.0	432.5	416.7	407.2
Wavelength (m)	1460	1131	875.3	700.3	583.0	497.8	432.5	378.8	339.3

Table 6.1: Measurements of phase velocity and wavelength as a function of frequency by picking maxima in Figure 6.5b.

EGFs shows there are few (to none) dominating and coherently acting noise sources. Thus the microseism noise at Ekofisk field is very suitable for creating Scholte-wave virtual seismic sources between 0.35 Hz to 1.35 Hz by seismic interferometry. I expect that crosscorrelating and stacking of more recorded data (had it been available) would increase the signal-to-noise-ratio (SNR) ratio.

A dispersion image is formed by taking the amplitude in the Radon domain, selecting all of the EGFs between station pairs with midpoints within UTM (513 – 514 km east, 6269 – 6270 km north) (denoted by a green square in Figure 6.1a), sorting these EGFs as a function of absolute offset (Figure 6.5a) and then slant stacking. Next, the data are transformed from the $\tau - p$ domain to the $\omega - p$ domain by Fourier transformation. The amplitudes are balanced over frequencies for clarity to produce Figure 6.5b. The fundamental Scholte-wave mode is the only mode visible in Figure 6.5b. It is a dispersive wavemode; i.e. the wavespeed varies with frequency. A summary of observed phase velocities as a function of frequency and their corresponding wavelengths is shown in Table 1. This table tells us that the microseism energy is not aliased in the in-line direction, but becomes aliased in the cross-line direction above 0.75 Hz.

The Scholte waves emitted by the virtual seismic sources propagate along the sea floor with wavelengths approximately between 1460 m at 0.4 Hz and 340 m at 1.2 Hz (from Figure 6.5b). These long wavelengths provide sensitivity away from the seabed, i.e. in depth. Lower frequencies will be more sensitive to deeper depths.

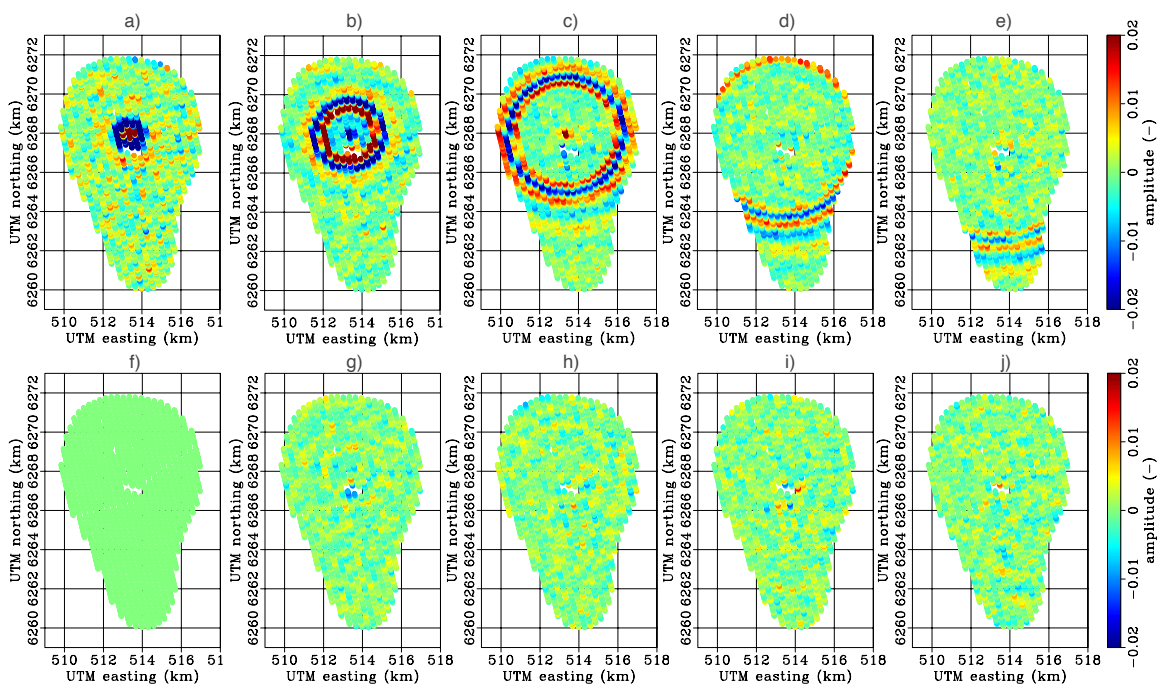


Figure 6.4: Snap shots for symmetric (a-e) and antisymmetric (f-j) parts of the EGFs. Correlation lags are 0s (a and f), 4s (b and g), 8s (c and h), 12s (d and i), and 16s (e and j). [CR] `ekofisk-shots`

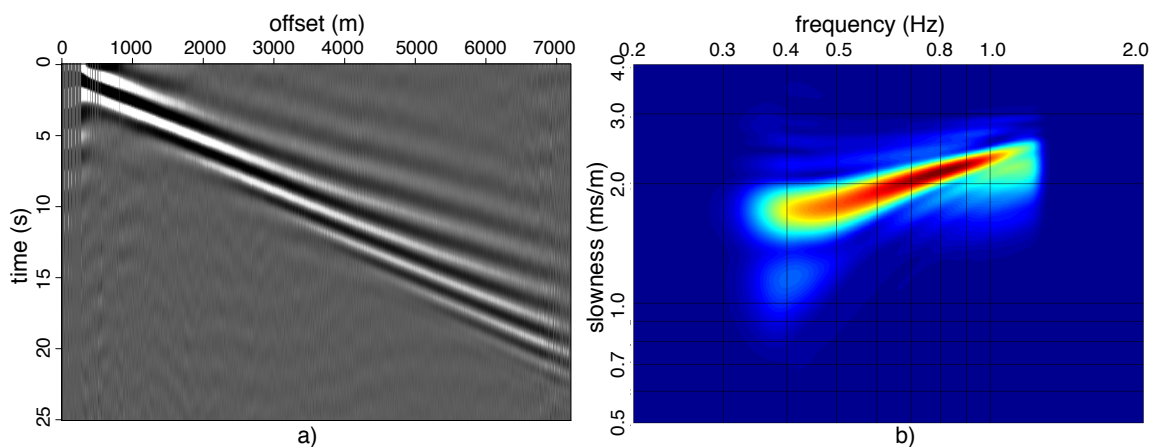


Figure 6.5: a) Offset gather for crosscorrelations between all station pairs with mid-points within UTM (513 – 514 km east, 6269 – 6270 km north). b) Dispersion image generated by transforming the gather in (a) to the $\omega - p$ domain and balancing the amplitude over frequencies. [CR] `gather-dispersion`

STRAIGHT-RAY TOMOGRAPHY FOR GROUP-VELOCITY MAPS

One way to image the Scholte waves emitted by the virtual seismic sources at Ekofisk is by group-velocity tomography. I use a straight-ray tomography kernel as before for virtual seismic sources at Valhall (Chapter 4).

After symmetrizing the EGFs, they are passed through a bandpass filter with a flat response over a 0.2 Hz interval and extending as Hann-tapers over an additional 0.2 Hz on either side. Travel times are picked as the envelope peak of the filtered EGFs. I again use the ratio between the maximum of the envelope within an estimated linear moveout window to the average of the envelope outside the window as a SNR quality factor.

The model space is formed by 90 (east-west) and by 140 (north-south) grid cells, 100 m by 100 m wide. The grid cell size is below the resolution of the wavelength, so the regularization plays an important role in finding reasonable solutions. The regularization strength, ϵ , is picked as a value above which the regularization has a significantly smaller smoothing effect (Aster et al., 2005).

Only stations with an SNR exceeding 2 and an offset exceeding 1500 m are selected (for smaller offsets the surface waves are not well developed) and all reciprocal stations are dropped (to keep one pick per station pair). Additionally, traveltimes pick residuals are filtered based on their corresponding velocity perturbation (the offsets divided by the traveltimes pick residuals); the smallest and largest 5% are discarded. The effect of discarding outliers before the inversion is minimal.

This whole procedure is repeated for five overlapping frequency ranges: 0.2 – 0.6 Hz, 0.4 – 0.8 Hz, 0.6 – 1.0 Hz, 0.8 – 1.2 Hz and 1.0 – 1.4 Hz. After inversion, the slowness map can be recovered from the perturbation map by adding the average slowness, $\mathbf{m} = \Delta\mathbf{m} + \mathbf{m}_0$. In Table 6.2 the number of selected traveltimes picks and their corresponding average velocities, \mathbf{m}_0^{-1} , are shown for each frequency range. Figure 6.6 contains the five maps found by solving the inverse problem. I observe a

Frequency range (Hz)	0.4 – 0.6	0.6 – 0.8	0.8 – 1.0	1.0 – 1.2	1.2 – 1.4
Number of traveltimes picks	1212778	5528579	5434445	3579255	552305
Average group velocity (m/s)	378.8	349.4	328.0	311.3	301.2

Table 6.2: Number of traveltimes picks used per inversion and their corresponding average velocity.

high-velocity anomaly in the center of the array, surrounded by a lower-velocity region. The high-velocity anomaly coincides with the center of the sea-floor subsidence bowl. Under the southern end of the array, where the magnitude of the gradient of the sea floor is smaller, I find higher velocities again.

Ekofisk’s LoFS has a dense concentration of stations resulting in a very good ray coverage and measurements throughout the domain of imaging (Figure 6.7a). This ray coverage is computed for all traveltimes picks used for the group-velocity tomography between 0.8 – 1.2 Hz (Figure 6.6c). One measure for resolution is a checkerboard test. I attempt to recover the checkerboard grid pattern shown in Figure 6.7b given the ray path coverage and the regularization strength. The difference between causal and anti-causal traveltimes picks was added as a proxy for the noise in the data (although its effect was negligible unless increased by two orders of magnitude). The edges of the recovered checkerboard grid cells are smoothed by the regularization (Figure 6.7c). The squares are not always well resolved at the edges of the array due to biased azimuthal coverage of the traveltimes picks. To see the effect of the chosen regularization parameter I image the final data misfit with the adjoint of the tomographic operator (Figure 6.7d). Most of the energy in the residual is an imprint of the acquisition geometry. There is also some energy that corresponds to geologically reasonable features. However, decreasing the regularization strength would make the acquisition imprint appear in the inverted model.

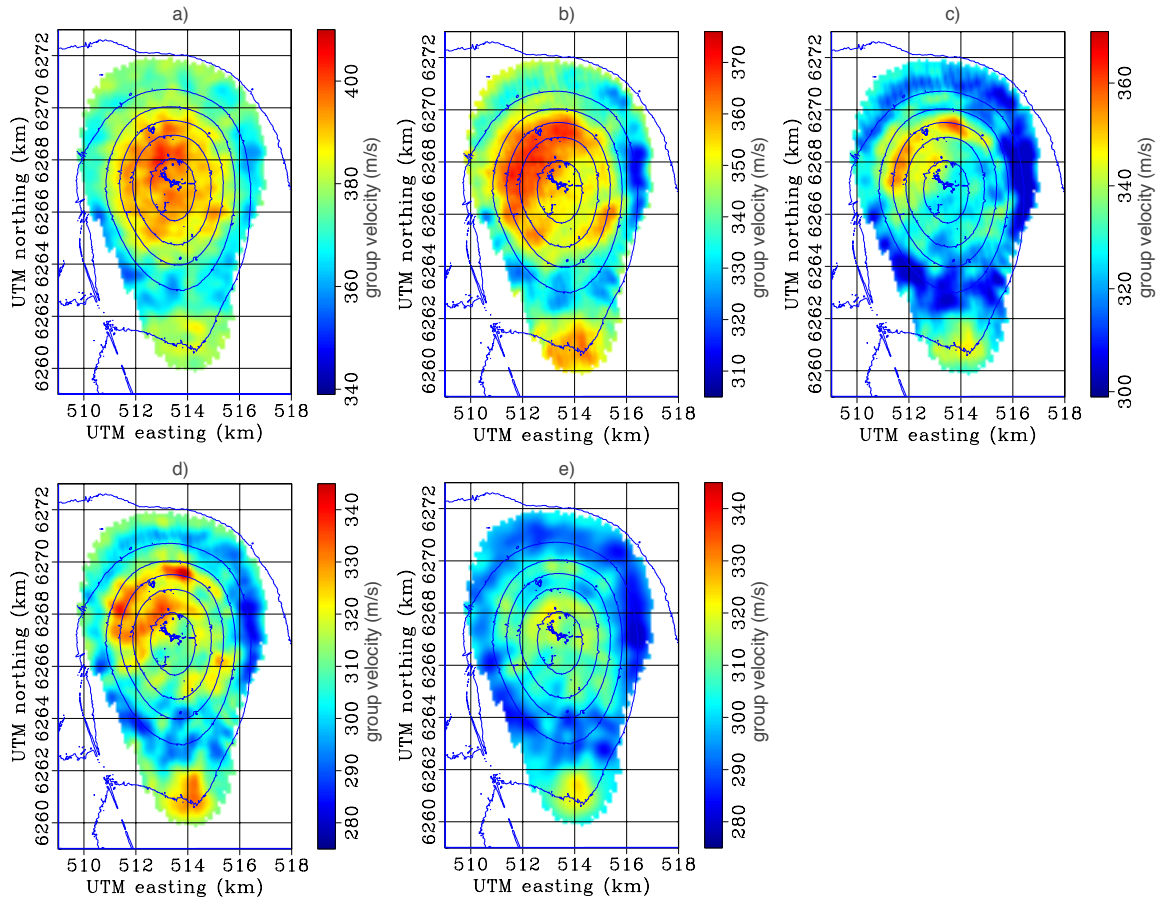


Figure 6.6: Straight-ray tomography maps for group velocities with center frequencies of 0.2 – 0.6 Hz in (a), 0.4 – 0.8 Hz in (b), 0.6 – 1.0 Hz in (c), 0.8 – 1.2 Hz in (d) and 1.0 – 1.4 Hz in (e). [CR] Ekofisk-straight-ray-tomo

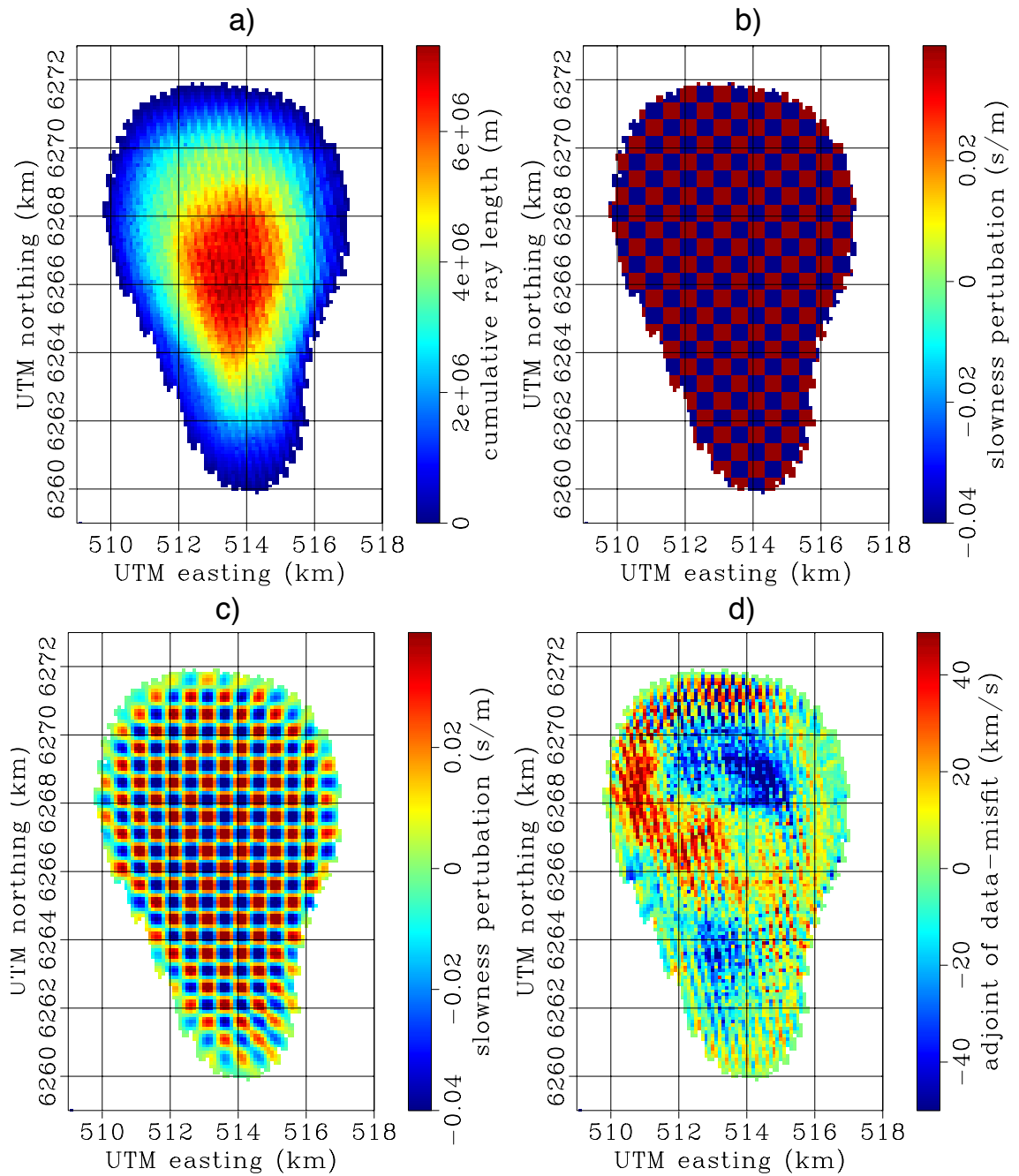


Figure 6.7: Resolution indicators for the Scholte-wave group-velocity images at central frequency range 0.8 – 1.2 Hz. a) cumulative ray-length through each cell, b) model checkerboard grid, c) retrieved checkerboard grid using the ray path coverage at (a). d) Adjoint of the tomographic operator applied to final data misfit. [CR] eko-resolution

DISCUSSION

Analysis of the ambient seismic noise recorded by the LoFS installed over Ekofisk field reveals swell-noise energy recorded below 0.35 Hz and microseism energy recorded between 0.35 – 1.35 Hz. The spectrogram in Figure 6.2 reveals that the swell-noise and swell-noise-generated microseism energy grew stronger during October 24th and remain strong during the 25th. I downloaded observations from a weather station at Ekofisk field (Weather Underground, Inc., 2013), and display the recorded barometric pressure at sea level and wind speeds in Figure 6.8. During October 24th and 25th I see

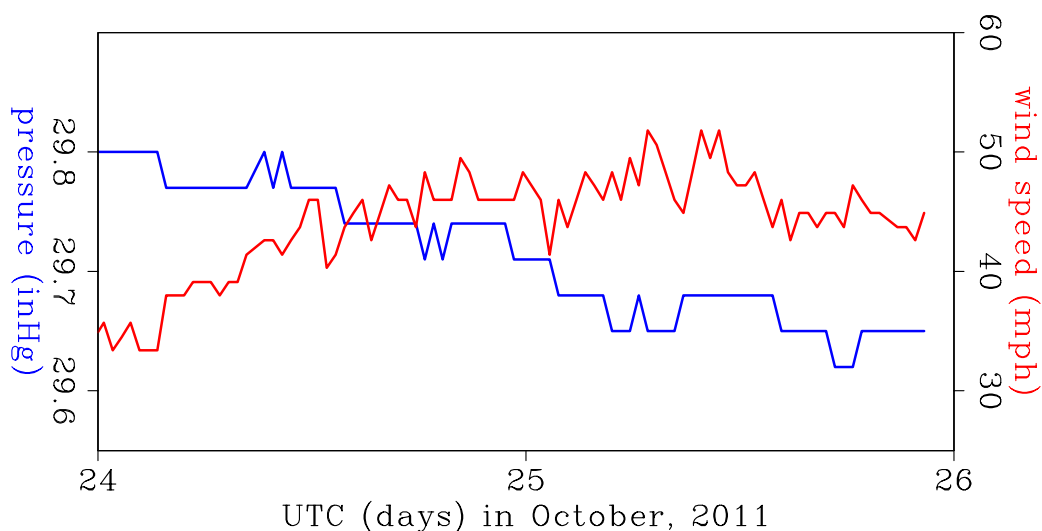


Figure 6.8: Measurements made by a weather-observation station at Ekofisk field (Weather Underground, Inc, 2013). Blue curve shows barometric pressure at sea level (in inHg). Red curve shows wind speed (in mph). [ER] weather

a gradual decrease in pressure, indicating the emergence or arrival of a low-pressure system, which is indicative of rougher weather conditions. This is corroborated by the increase in wind-strengths during the 24th, and wind generally remains strong during the 25th. This correlation between weather conditions and microseism energy levels at Ekofisk field is not guaranteed because sea-swell-excited microseism energy could be generated quite far from Ekofisk field. However, I find that to first order, microseism nose is incident from all directions equally during the duration of the recording (Figure 6.3). This indicates that weather conditions were probably the

same for the entire North Sea and that the recording at Ekofisk field is representative for the weather that excited the microseism noise for the duration of the recording. This omni-directional microseism noise is very favorable for seismic-interferometry (Weaver and Lobkis, 2002; Wapenaar and Fokkema, 2006). From comparisons with beam steering experiments in Chapter 2 on four recordings made during October, December, January and February at Valhall field, I know this may be representative of microseismic-energy conditions in the North Sea during fall and winter.

Omnidirectional microseismic noise translates into omnidirectional virtual seismic sources. The resulting virtual seismic sources at Ekofisk field, where no balancing was applied before stacking crosscorrelations from different time-windows, is almost perfectly symmetric. There is almost no observable antisymmetric part to the cross-correlation stacks, and the background correlation fluctuations in the antisymmetric part of the crosscorrelations are of the same strength as in the symmetric part. These background fluctuations will diminish when crosscorrelating and stacking more ambient seismic recordings (de Ridder and Biondi, 2012), provided they are made under similar conditions.

The virtual seismic sources are dominated by a single dispersive wave mode, corresponding to the fundamental Scholte-wave mode. The Scholte waves are well formed between 0.4 Hz and 1.2 Hz, and they have wavelengths as short as 340 m at the upper end of the frequency band and as long as 1460 m at the lower end. Based on an approximate peak sensitivity at their half-wavelength they should exhibit depth sensitivity between 170 m to 565 m below the sea floor (Aki and Richards, 2002).

Group-velocity images generally show a high-velocity anomaly coinciding with the center of the sea-floor subsidence. At the southern end of the array, there is a high-velocity region again. I considered whether the high anomaly could be caused by the flat sea floor approximation. Referring to Figure 6.1, a subsidence of 9 m over approximately 2 km horizontal distance, disproves that this velocity of 20 m/s could be caused by the flat-earth approximation. This pattern holds over multiple central frequency ranges, which can be an indication that it is not reflective of geology but of stress-patterns that carry across lithological boundaries.

In the group-velocity map from the highest frequency band (Figure 6.6e), one can see that the low velocities form a ring surrounding the sea-floor subsidence (Figure 6.1b). I generally find higher Scholte-wave group velocities where the sea-floor gradient is low, and lower Scholte-wave group velocities where the sea-floor gradient is high. They are likely related to the stress state in the overburden. Similar anomalies have been found at Valhall field from critically reflected P-waves (Hatchell et al., 2009).

Crosscorrelating longer time recordings should increase the signal-to-noise ratio, especially at the upper end of the frequency range. Different noise conditions, potentially under heavy weather, can increase the signal in the lower end and upper end of the microseism frequency range. Depending on exact processing and inversion schemes, group-velocity images from ambient seismic noise are remarkably stable from recordings as short as a day (de Ridder and Biondi, 2013).

CONCLUSIONS

In this chapter I show that the microseism noise in the ambient seismic field between 0.4 and 1.2 Hz, as recorded by Ekofisk's LoFS array, is suitable for retrieval of Scholte waves by seismic interferometry. The microseism energy at Ekofisk field in this recording is particularly uniformly distributed over azimuth and thus ideal for seismic interferometry. Dispersive virtual seismic sources emitting Scholte-waves between 0.4 and 1.2 Hz are retrieved by passive seismic interferometry. The interface waves should exhibit an approximate peak depth sensitivity between 170 m to 730 m below the sea floor. Scholte-wave group-velocity tomography locates a high-velocity anomaly in the center of the array, surrounded by a lower-velocity region. The high-velocity anomaly coincides with the center of the sea-floor subsidence bowl. The ring of lower velocities corresponds with high magnitudes of the bathymetry gradient. Under the the southern end of the array, I find higher velocities again. This behavior may reflect overburden stress states caused by decades of production and reservoir depletion.

ACKNOWLEDGMENTS

My thanks to ConocoPhillips Skandinavia AS and the PL018 Partnership (Total E&P Norge AS, ENI Norge AS, Statoil Petroleum AS and Petoro AS) for access to Ekofisk data, and for permission to publish these results. My thanks to Olaf Knoth, Ali Tura, Alexandre Bertrand, Roman Kazinnik and Lars Vedvik of ConocoPhillips for helpful discussions and suggestions and for accessibility to the data. I thank Stewart Levin for his expertise on SEG-D formats and help reading the data and meticulously decoding the header fields.